International Conference on Space Optics—ICSO 2014

La Caleta, Tenerife, Canary Islands

7–10 October 2014

Edited by Zoran Sodnik, Bruno Cugny, and Nikos Karafolas

Radiometric assessment method for diffraction effects in hyperspectral imagers applied to the earth explorer #8 mission candidate flex

R. Berlich

B. Harnisch

International Conference on Space Optics — ICSO 2014, edited by Zoran Sodnik, Nikos Karafolas, Bruno Cugny, Proc. of SPIE Vol. 10563, 1056354 · © 2014 ESA and CNES
CCC code: 0277-786X/17/$18 · doi: 10.1117/12.2304079

RADIOMETRIC ASSESSMENT METHOD FOR DIFFRACTION EFFECTS IN HYPERSPECTRAL IMAGERS APPLIED TO THE EARTH EXPLORER #8 MISSION CANDIDATE FLEX

R. Berlich[1], B. Harnisch[2]
[1]*Berlich Optical Systems Engineering, Jena, Germany, berlich@opticalengineering.de*
[2]*ESA/ESTEC, Noordwijk, The Netherlands, bernd.harnisch@esa.int*

Abstract **- An accurate stray light analysis represents a crucial part in the early design phase of hyperspectral imaging systems, since scattering effects can severely limit the radiometric accuracy performance. In addition to conventional contributors including ghost images and surface scattering, i.e. caused by a residual surface micro-roughness and particle contamination, diffraction effects can result in significant radiometric errors in the spatial and spectral domain of pushbroom scanners. In this paper, we present a mathematical approach that efficiently evaluates these diffraction effects based on a Fourier analysis. It is shown that considering the conventional diffraction at the systems entrance pupil only, significantly overestimates the stray light contribution. In fact, a correct assessment necessitates taking into account the joint influence of the entrance pupil, the spectrometer slit as well as the dispersion element. We quantitatively investigate the corresponding impact on the Instrument Spectral Response Function (ISRF) of the Earth Explorer #8 Mission Candidate FLEX and analyse the expected radiometric error distribution for a typical earth observation scenario requirement.**

I. INTRODUCTION

Hyperspectral imaging constitutes a key technology within state-of-the-art earth observation systems. Particular missions currently operating include EO-1/Hyperion, PROBA/CHRIS and HICO [1-4]. In addition, several candidates such as EnMAP, PRISMA, and FLORIS/FLEX are currently under development or in planning stage [1,5-7]. The corresponding optical instruments are based on pushbroom type configuration, which enable extended acquisition of spatial as well as spectral information. The accurate radiometric measurement of corresponding spectral bands with high spectral resolution requires stringent requirements on the systems stray light performance. Crucial stray light contributors that already need to be assessed in the early design phase are ghost images due to multiple reflections on optical surfaces, surfaces scattering effects, as well as diffraction. Whereas the former two can be assessed in detail using comprehensive raytracing software packages, the analysis of diffraction effects often relies on incorporating simplified analytical models. Conventional approaches are based on a convolution with the system's Point Spread Functions (PSF), which is determined by diffraction at the entrance pupil. However, this approach is not valid for pushbroom type setups. In fact, the shift-invariance condition is violated due to the slit in combination with the grating dispersion. The conventional diffraction limited PSF can consequently not be applied to analyse the radiometric system performance.
In this paper, we introduce an analytical approach that takes into account diffraction at the entrance pupil, the spectrometer slit as well as the dispersion element. It allows for a simplified assessment of hyperspectral imaging systems and provides an estimate of the expected radiometric accuracy limitations. By applying the model to investigate diffraction effects of FLORIS, the optical payload of the Earth Explorer #8 Mission Candidate FLEX [6,7], we show that an analysis based on the diffraction limited PSF significantly overestimates the corresponding stray light error.

II. METHOD DESCRIPTION

A. System configuration and assumptions

The considered optical system is based on the idealized configuration shown in Fig. 1 in order to allow for an analytical investigation of the complex pushbroom setup. Note that the x- and y-coordinates correspond to the across- and along-track directions, respectively. The idealized system enables focussing the evaluation on the main diffraction effects by neglecting other effects such as aberrations and scattering of light at optical surfaces. The involved imaging components, namely the telescope, the spectrometer collimator and the spectrometer imager are idealized by paraxial lenses. The dispersion element is exemplarily represented by a grating operating in reflection or transmission condition. It is assumed that the paraxial lenses are infinitely extended in the lateral dimensions and do not lead to additional diffraction effects. The same assumption applies for the (across track) length of the spectrometer slit. In fact, diffraction effects during the light propagation through the system are reduced to three contributors, the entrance pupil, the (along track) slit width and the grating aperture. Additionally, all apertures (including the slit) are assumed to have a negligible thickness and the transmission (or reflection) of

all optical components is idealized to be equal to 1. Finally, it is assumed the Fraunhofer approximation can be applied to describe the optical imaging system (excluding the grating).

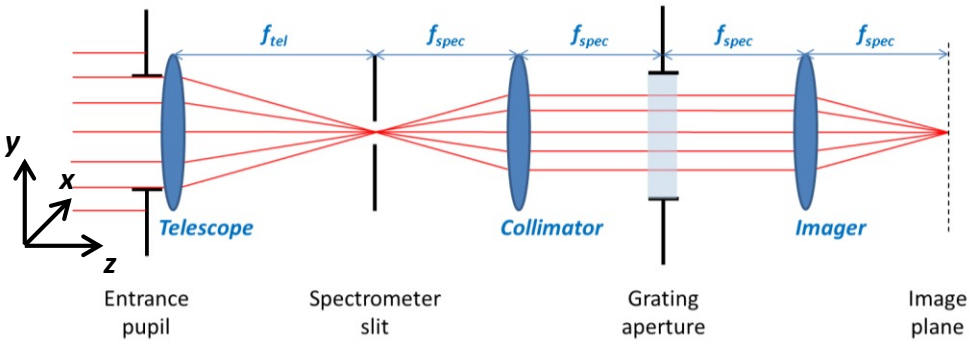

Fig. 1. Considered idealized pushbroom configuration and corresponding coordinate system.

B. System propagation

The analytical calculation approach utilizes the Fourier relationship of the optical fields $u(x,y)$ between the different planes of the imaging configuration. It enables fast propagation of the light distribution through the entire optical system while taking into account the different diffraction effects at the limited apertures. Fig. 2 illustrates the field distributions in the corresponding spatial and angular (or spatial frequency) domain at each individual propagation step. Both domains are related with each other by a Fourier transformation.

$$u'(k_x, k_y) = FT[u(x,y)] \tag{1}$$

Only the one-dimensional (along track) propagation is illustrated while the actual calculation considers the complete two-dimensional field distribution. Note that the particular FLORIS parameters as presented in Tab. 1 are exemplarily applied for illustration purposes. The collimated, on-axis field impinging the entrance pupil of the telescope with a wavelength λ_0 is characterized by a homogeneous spatial extension and a delta-distribution in the angular domain. The circular entrance pupil aperture of diameter d_{EP} initially truncates this field, which leads to a broadening in angular space. Next, the resulting field is propagated into the telescope focal plane by applying a Fourier transformation. The relationship between the entrance pupil's angular domain and the focal planes spatial domain is given by [8]

$$(x,y) = \frac{\lambda_0 \cdot f_{tel} \cdot (k_x, k_y)}{2\pi} \tag{2}$$

The field is subsequently truncated in the spatial domain (in one-dimension) due to the finite slit width s which causes a broadening in the corresponding angular domain. An additional Fourier transformation is performed to propagate the field behind the spectrometer slit into the grating plane. The angular coordinates are determined by the spectrometer focal length f_{spec} according to

$$(k_x, k_y) = \frac{2\pi \cdot (x,y)}{\lambda_0 \cdot f_{spec}} \tag{3}$$

Subsequently, the field interaction with the grating is based on two main effects. The deflection of the incident wave into the anticipated diffraction order corresponds to a linear shift of the field in the angular domain, which eventually results in a transversal shift of the final image. The influence can be omitted within the idealized assessment by considering a proper coordinate transformation. The second effect originates from the limited grating aperture and leads to a respective field truncation in the spatial domain. Although the grating aperture is generally well oversized with regard to the FWHM spatial field extension, a small fraction of the outer wings is still cutoff by the aperture. It should be emphasized that these wings originate from the field truncation at the spectrometer slit and they can be referred to diffraction effects of the slit. The resulting broadening in the angular domain is only minor as can be seen in Fig. 2. A final Fourier transformation is performed, which propagates the field behind the grating into the spectrometer focal plane. Taking the absolute square of the field ultimately yields the image plane irradiance distribution

$$E(x,y,\lambda_0) = |u(x,y,\lambda_0)|^2 \tag{4}$$

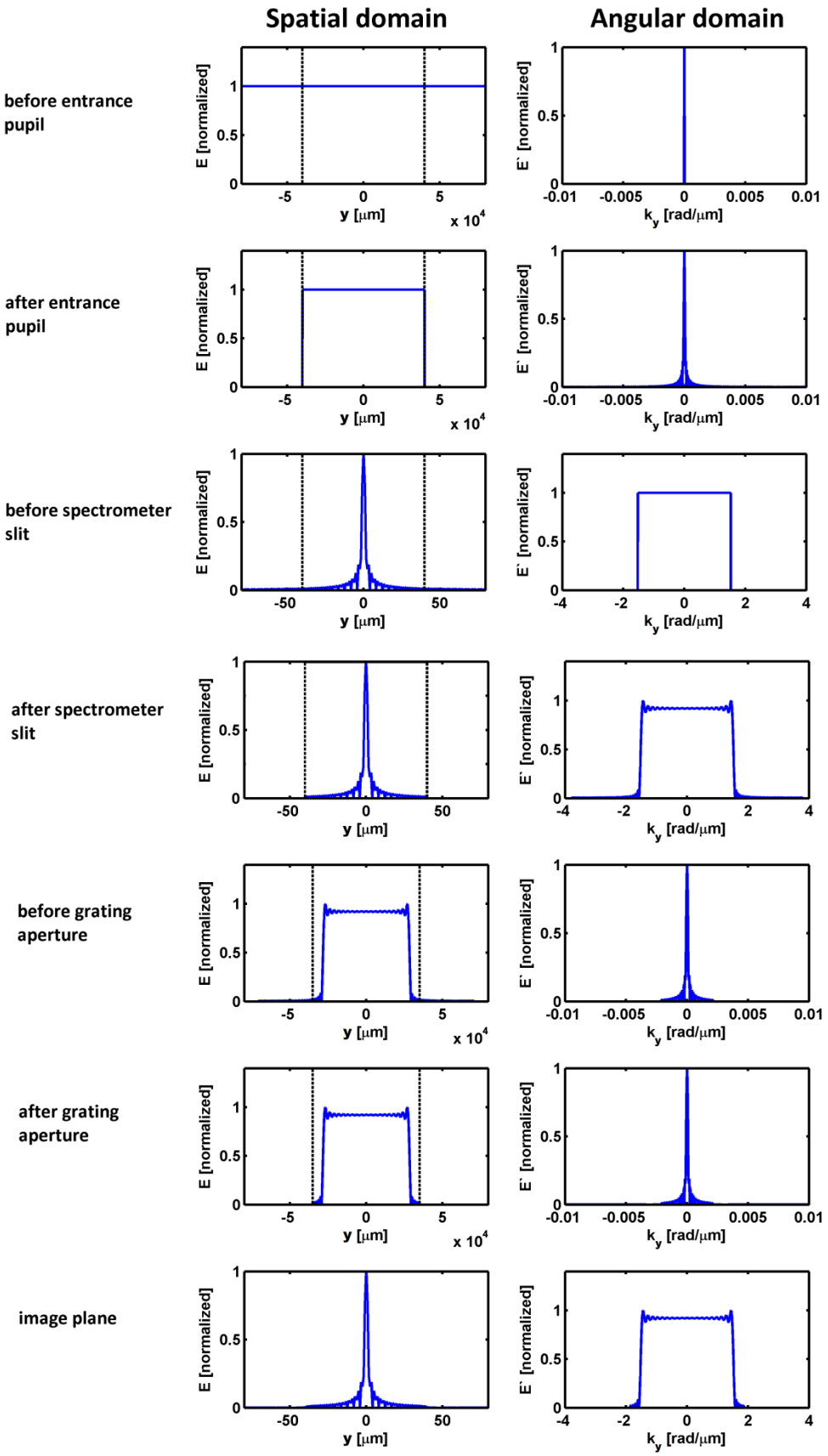

Fig. 2. Individual steps of the analytical method to assess diffraction effects in pushbroom type systems. The square modulus of the field distributions in the spatial and angular domain are plotted in each plane. Note that both domains are related by a Fourier transformation. Dashed lines denote the respective aperture sizes.

C. Line Source Response Function

The described approached so far only considered a single point source. The proper radiometric assessment however necessitates the consideration of extended scene radiance distributions. Consequently, a set of multiple point sources needs to be traced through the system. In fact, the assessment can be limited to a one dimensional line of point sources in the along track direction (y-direction), since the system (including the slit) is shift-invariant in the across track direction (x-direction). Thus, the image plane irradiance can be written as a superposition

$$E(x_{im}, y_{im}, \lambda_0) = I_0 \cdot \sum_{i=-N/2}^{N/2} E_i(x_{im}, y_{im}, \lambda_0) = I_0 \cdot \sum_{i=-N/2}^{N/2} O\left[\delta\left(x_{obj}, y_{obj} - i \cdot a, \lambda_0\right)\right] \tag{5}$$

The operator O denotes the imaging process based on the previously described approach. The corresponding point source spacing a should be smaller than (or in the order of) the systems PSF extension with respect to object space. Eventually, the constant factor I_0 normalizes the total power. In the following, $E(x_{im}, y_{im}, \lambda_0)$ is referred as the systems Line Source Response Function (LSRF).

$$LSRF(x_{im}, y_{im}, \lambda_0) \doteq I_0 \cdot \sum_{i=-N/2}^{N/2} O\left[\delta\left(x_{obj}, y_{obj} - i \cdot a, \lambda_0\right)\right] \tag{6}$$

It is emphasized that a finite number of N point sources that extend over approximately three slit widths describe $LSRF$ with sufficient accuracy. Fig. 3 illustrates the corresponding calculation approach in two dimensions. A set of (incoherent) point sources (red dots) is placed in object space and subsequently imaged into the telescope focal plane. The obtained diffraction limited pattern is then truncated by the slit extension (black rectangle), which blocks part of the diffracted light. Finally, this distribution is imaged through the spectrometer and results in the diffraction limited image distribution of the point source assembly, defined as $LSRF$.

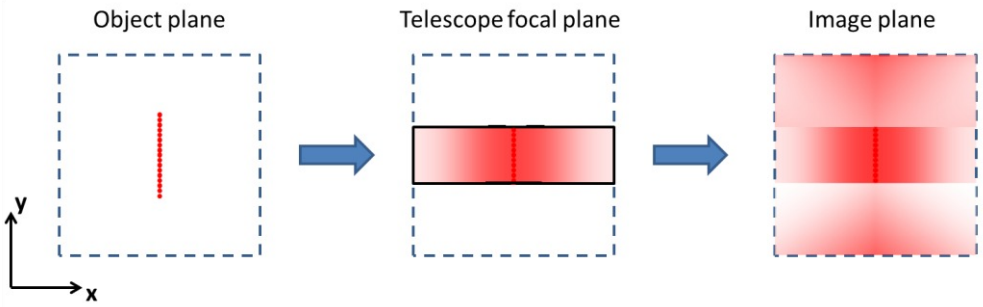

Fig. 3. Schematic approach to calculate $LSRF$ by imaging a linear set of point sources.

The y_{im}-coordinate in the $LSRF$ definition corresponds to the particular wavelength λ by

$$y_{im}(\lambda) = (\lambda - \lambda_M)\frac{\Delta y}{\Delta \lambda} \tag{7}$$

according to the considered linear grating dispersion. Here, λ_M denotes the wavelength that corresponds to the on-axis image position $y_{im} = 0$. Moreover, Δy represents the linear position shift in image space for a wavelength difference of $\Delta\lambda$. In fact, $LSRF$ can be considered as a two-dimensional Instrument Spectral Response Function (ISRF), which can be obtained by integrating the $LSRF$ over the across track direction

$$ISRF(\lambda, \lambda_0) = \int LSRF(x_{im}, y_{im}(\lambda), \lambda_0)\, dx_{im} \tag{8}$$

Note, $LSRF(x_{im}, y_{im}(\lambda), \lambda_0)$ does not include the effect of the finite pixel size yet. However, it can easily be accounted for by an additional convolution with the rectangular pixel shape.

D. Radiometric accuracy

The radiometric error due to diffraction, which can also be referred to the radiometric accuracy, is defined by the relative difference

$$\eta(x_{im}, y_{im}) = \frac{\bar{E}_{diff}(x_{im}, y_{im}) - \bar{E}_n(x_{im}, y_{im})}{\bar{E}_n(x_{im}, y_{im})} = \frac{\int E_{diff}(x_{im}, y_{im}(\lambda_0), \lambda_0)\, d\lambda_0 - \int E_n(x_{im}, y_{im}(\lambda_0), \lambda_0)\, d\lambda_0}{\int E_n(x_{im}, y_{im}(\lambda_0), \lambda_0)\, d\lambda_0} \quad (9)$$

where $E_n(x_{im}, y_{im}(\lambda_0), \lambda_0)$ denotes the nominal spectral image irradiance if no diffraction would be present and $E_{diff}(x_{im}, y_{im}, \lambda_0)$ defines the spectral image irradiance in the presence of diffraction. Both can be obtained as follows. Initially, the projection of the object radiance distribution $L(x_{obj}, \lambda_0)$ into the systems image plane is considered. Note that the x-dependency can be omitted since $L(x_{obj}, y_{obj}, \lambda_0)$ must be invariant in the along-track direction. According to [8], E_0 can be approximated by

$$E_0(x_{im}, \lambda_0) \cong \frac{\pi}{4F_{\#}^2} \cdot L\left(M_x \cdot x_{obj}, \lambda_0\right) \quad (10)$$

considering the system's F-number $F_{\#}$ and the in-field object radiance distribution $L(x_{obj}, \lambda_0)$. The system's across track magnification is denoted by M_x. On the one hand, $E_n(x_{im}, y_{im}, \lambda_0)$ is given inside the slit extension s by considering (7)

$$E_n(x_{im}, y_{im}, \lambda_0) = \begin{cases} E_0(x_{im}, \lambda_0) & \text{for } \left| y_{im} - (\lambda_0 - \lambda_M)\frac{\Delta y}{\Delta \lambda} \right| \le s \\ 0 & \text{otherwise} \end{cases} \quad (11)$$

On the other hand, $E_{diff}(x_{im}, y_{im}(\lambda_0), \lambda_0)$ is obtained by a convolution

$$E_{diff}(x_{im}, y_{im}, \lambda_0) = \int E_0(x'_{im}, \lambda_0) \cdot LSRF\left(x_{im} - x'_{im}, y_{im} - (\lambda_0 - \lambda_M)\frac{\Delta y}{\Delta \lambda}, \lambda_0\right) dx'_{im} \quad (12)$$

where $LSRF$ is normalized by

$$\iint LSRF(x_{im}, y_{im}, \lambda_0) dx_{im} dy_{im} = 1 \quad (13)$$

It is important to emphasize again that convolution (12) can only be applied for object radiance distributions $L(x_{obj}, y_{obj}, \lambda_0)$ which are **invariant in the along-track (y-) direction**. Otherwise, $LSRF$ as derived in the previous section cannot be applied and a more complex calculation model must be developed.

III. DIFFRACTION LIMITATION ASSESSMENT OF FLORIS

A. System parameters

Tab. 1. Basic geometrical and optical properties of the simplified FLORIS model.

Parameter	Parameter variable	Value
Entrance pupil diameter	d_{EP}	80 mm
Telescope focal length	f_{tel}	217 mm
Slit width	s	80 µm (1 SSD)
Spectrometer focal length	f_{spec}	154 mm
Grating diameter	d_G	70 mm
Wavelength	λ_0	760 nm
Pixel size	p_x x p_y	80 µm x 28 µm

The basic geometrical and optical properties [6,7], which are considered for the assessment of the diffraction limitations of FLORIS, are summarized in Tab. 1. Note that they serve for demonstration purposes for the method presented in this paper and do not necessarily reflect the current system baseline within the FLEX mission development.

B. LSRF calculation

The two-dimensional $LSRF$ is calculated with the presented method considering the optical system of FLORIS. The corresponding results are shown in Fig. 4 (a). The particular distribution illustrates the results of the involved diffraction effects. On the one hand, the part of the $LSRF$ inside the slit extension ($|y| \leq 40\mu m$) is mainly subject to diffraction at the entrance pupil of the system. On the other hand, the area outside refers to diffraction effects of the slit and the limited grating aperture. It can be seen that the irradiance decreases severely faster in y-direction than in x-direction. This observation demonstrates that the slit severely reduces the telescopes diffracted (stray-) light and only contributes a small amount of diffracted light itself. In order to illustrate the difference to the assessment approach based on the conventional diffraction at the entrance pupil, the corresponding PSF is plotted in Fig. 4 (b). It can be seen that the irradiance in the y-direction is severely increased. Consequently, the stray light contribution is significantly overestimated.

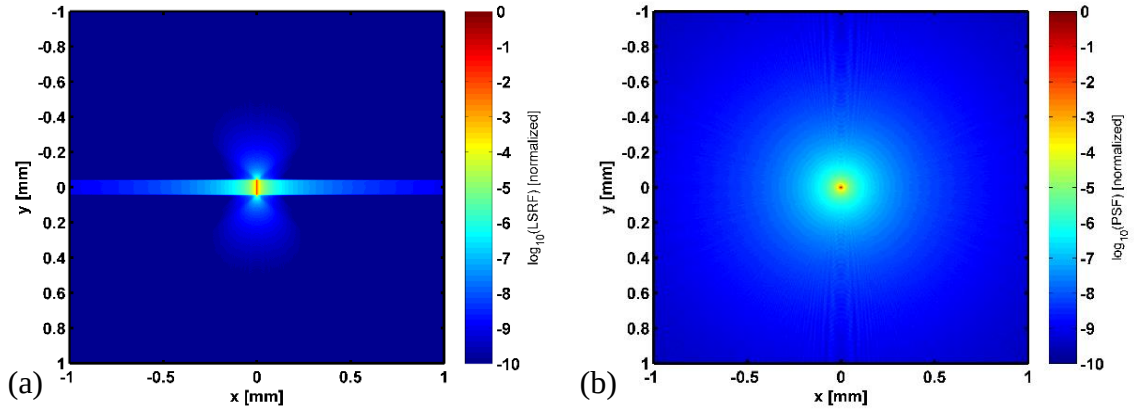

Fig. 4. (a) Calculated Line Source Response Function of the considered optical system of FLORIS based on the presented calculation method. (b) Diffraction limited point spread function omitting the effect of the slit.

C. Object radiance distribution

The incorporated spatial and spectral distributions of the object scene are illustrated in Fig. 5 in accordance with the requirement defined in [6]. In particular, an object scene with a 20 SSD wide cloud gap in the centre of the field of view is assumed. Only the in-field (500SSD) and in-band spatial and spectral radiance extension of the crucial O2A band (740nm-780nm) are considered. The spectrum is convolved with a 0.3 nm wide Gaussian distribution according to the spectral resolution and sampled with 1 $SSI = 0.1\ nm$.

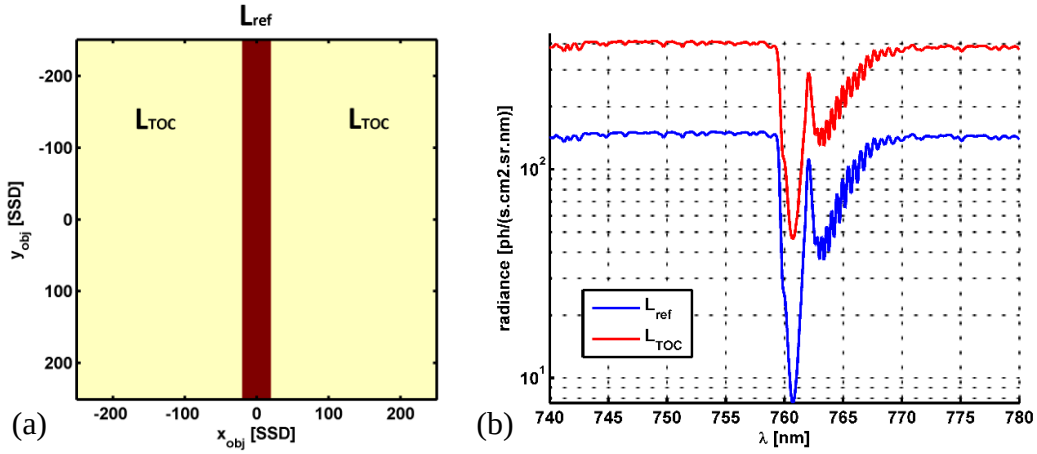

Fig. 5 (a) Spatial and (b) spectral object radiance distribution under consideration according to [6]. A cloud gap of 20SSD width is assumed. The O2A band is convolved with a 0.3nm wide Gaussian distribution.

D. Radiometric error

In order to calculate the convolution integral (12), the two-dimensional $LSRF$ must be resampled according detector pixel grid. In this respect, it is convolved with the 80 x 28 µm^2 pixel extension. Furthermore, it is assumed that the line source response function does not significantly change within the considered wave band, which allows the use of a single, representative $LSRF$ at $\lambda_0 = 760\ nm$. Under these assumptions, the final nominal irradiance distribution E_n as displayed in Fig. 6 (a) is obtained in image space. Note that the y-axis is converted to the corresponding wavelength scale according to (7). The comparison with the diffraction limited irradiance E_{diff} reveals the radiometric error as defined in (9). The corresponding distribution is illustrated in Fig. 6 (c). It can be observed that the error is negligible for the wavelength range outside to absorption gap due to the homogeneous spectral plateau distribution. Conversely, the radiometric error is significant for spatial samples inside the cloud gap and in the proximity of the absorption peak at 761 nm. Two main effects can be identified that determine the particular error distribution. The strongly fluctuating peaks in the order of 0.5% can be referred to short-range effects that originate from the local modulation of the considered object spectrum as can be seen in Fig. 5 (a). Negative errors are accordingly obtained for local wavelength peaks where the energy is diffracted into the adjacent spectral samples with a lower radiance. Conversely, the positive peaks correspond to local radiance dips which are mainly influenced the additional radiance contribution from adjacent spectral samples. The second effect is of longer range and originates from stray light, which is diffracted from regions outside the absorption gap inside the 761 nm area. The cross section inside the cloud gap at $x_{im} = 0$, which is plotted in Fig. 6 (b), reveals that both effects are in the same order and lead to a maximum radiometric error of approximately 0.5%. It can thus be concluded that the range of diffraction induced errors is very narrow due to the rapid decrease of the LSRF, i.e. in the spectral direction. For comparison, Fig. 6 (b) and (d) show the radiometric error distribution in case the object radiance is convolved with the diffraction limited point spread function. The distribution inside the absorption gap exhibits the same fluctuations due to short range diffraction effects in the order of 0.5%. However, a significant peak at 761 nm is obtained with a maximum error of 2.2 %, which can be referred to the long-range effects. Consequently, the PSF approach clearly overestimates the radiometric error and the long-range effects in particular.

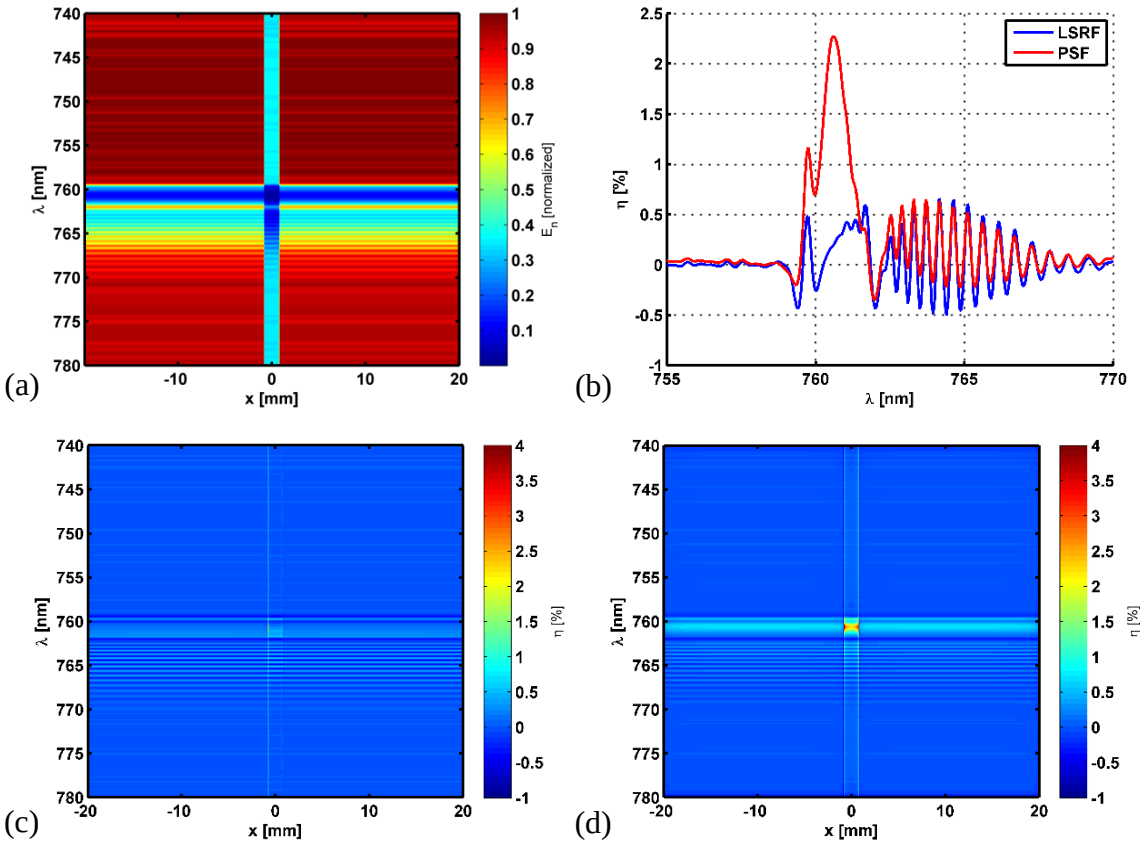

Fig. 6. (a) Nominal image plane irradiance distribution. (b) Radiometric error cross section at $x_{im} = 0$. The red and blue curves are calculated by a convolution of the object scene with the LSRF and the PSF, respectively. (c) and (d) respectively show the 2D error distribution based on a convolution with the LSRF and the PSF.

IV. CONCLUSION

In conclusion, a method was presented which enables estimating stray light caused by diffraction effects within hyperspectral imaging systems. The considered pushbroom type system is idealized in order to allow for an analytical assessment. The approach utilizes the Fourier relationship between different planes of the imaging configuration and thus permits a fast and efficient investigation of diffraction effects. We emphasize that it is not sufficient to exclusively consider the diffraction at the entrance pupil by a simple point spread function (PSF) evaluation. In fact, the presented model permits the assessment of the combined contribution of diffraction from the entrance pupil, the spectrometer slit and the grating aperture. In this context, the line source response function (LSRF) was defined, which can be referred as a two-dimensional, diffraction limited Instrument Spectral Response Function (ISRF). It was eventually demonstrated how the LSRF can be utilized to efficiently evaluate the radiometric accuracy based on a convolution with the object scene.

The developed model was applied to predict the radiometric error caused by diffraction effects for the particular optical system of FLORIS. A maximum error of approximately 0.5 % was determined considering the specific scenario defined by the system requirements [6]. It was shown that the range of diffraction induced errors is very narrow due to the rapid decrease of the LSRF. An additional comparison revealed that the error calculation based on a simple PSF evaluation overestimates the diffraction error, i.e. with respect to the long-range spectral stray light contribution.

Finally, it is emphasized that the results obtained by incorporating the presented method provide a first estimate of the actual diffraction error, which can particularly serve for the establishment of a reasonable stray light budget. Moreover, the approach is considered to provide a basis for the development of adequate image post-processing routines to mitigate the diffraction errors by a potential deconvolution.

REFERENCES

[1] K. Staenz, A. Mueller, and U. Heiden, "Overview of terrestrial imaging spectroscopy missions," *IGARSS*, pp. 1–4, 2013.

[2] M. Folkman and J. Pearlman, "EO-1/Hyperion hyperspectral imager design, development, characterization, and calibration," *Proceedings of SPIE*, vol. 4151, no. 2001, 2001.

[3] M. Barnsley and J. Settle, "The PROBA/CHRIS mission: A low-cost smallsat for hyperspectral multiangle observations of the earth surface and atmosphere," *IEEE TRANSACTIONS ON GEOSCIENCE AND REMOTE SENSING*, vol. 42, no. 7, pp. 1512–1520, 2004.

[4] R. L. Lucke, M. Corson, N. R. McGlothlin, S. D. Butcher, D. L. Wood, D. R. Korwan, R. R. Li, W. a Snyder, C. O. Davis, and D. T. Chen, "Hyperspectral Imager for the Coastal Ocean: instrument description and first images.," *Applied optics*, vol. 50, no. 11, pp. 1501–16, Apr. 2011.

[5] T. Stuffler, C. Kaufmann, S. Hofer, K. P. Förster, G. Schreier, A. Mueller, A. Eckardt, H. Bach, B. Penné, U. Benz, and R. Haydn, "The EnMAP hyperspectral imager—An advanced optical payload for future applications in Earth observation programmes," *Acta Astronautica*, vol. 61, no. 1–6, pp. 115–120, Jun. 2007.

[6] S. Kraft, J.-L. Bézy, U. Del Bello, R. Berlich, M. Drusch, R. Franco, A. Gabriele, B. Harnisch, R. Meynart, and P. Silvestrin, "FLORIS: phase A status of the fluorescence imaging spectrometer of the Earth Explorer mission candidate FLEX," *Proc. of SPIE*, vol. 8889, p. 88890T, Oct. 2013.

[7] S. Kraft, U. Del Bello, M. Drusch, a. Gabriele, B. Harnisch, and J. Moreno, "On the demands on imaging spectrometry for the monitoring of global vegetation fluorescence from space," *Proc. of SPIE*, vol. 8870, p. 88700N, Sep. 2013.

[8] M. Born, E. Wolf, *Principles of Optics: Electromagnetic Theory of Propagation, Interference and Diffraction of Light*, 7rd ed., CUP Archive, 1999.